Effects of residual stresses on fatigue crack propagation of an orthotropic steel bridge deck

van den Berg, Niels; Xin, Haohui; Veljkovic, Milan

DOI
10.1016/j.matdes.2020.109294

Publication date
2021

Document Version
Final published version

Published in
Materials and Design

Citation (APA)
van den Berg, N., Xin, H., & Veljkovic, M. (2021). Effects of residual stresses on fatigue crack propagation of an orthotropic steel bridge deck. *Materials and Design*, *198*, 1-19. Article 109294. https://doi.org/10.1016/j.matdes.2020.109294

Materials and Design 198 (2021) 109294

Contents lists available at ScienceDirect

Materials and Design

journal homepage: www.elsevier.com/locate/matdes

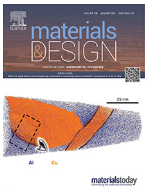

Effects of residual stresses on fatigue crack propagation of an orthotropic steel bridge deck

Niels van den Berg [a], Haohui Xin [b,a,*], Milan Veljkovic [a]

[a] *Faculty of Civil Engineering and Geosciences, Delft University of Technology, Netherlands*
[b] *Department of Civil Engineering, School of Human Settlements and Civil Engineering, Xi'an Jiaotong University, Xi'an, Shaanxi 710049, China*

HIGHLIGHTS

- A FE model including shrinkage due to welding has been made to predict and validate the residual stress field of the OSD.
- The fatigue crack simulation including residual stress field shows good correlation compared to the experimental data, while the simulation without residual stress field shows less correlation.
- The effects of the residual stresses are relatively large as the tensile transversal residual stresses increase the crack propagation, while the tensile longitudinal residual stresses decrease the crack propagation rate.

GRAPHICAL ABSTRACT

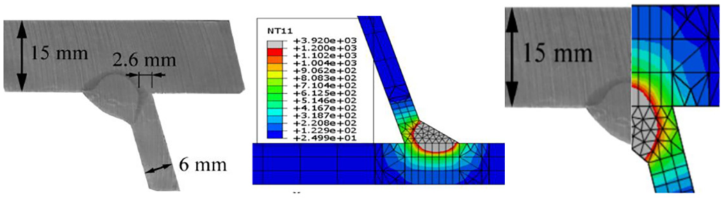

Residual Stress distribution

Crack Shape Comparisons

ARTICLE INFO

Article history:
Received 10 May 2020
Received in revised form 18 October 2020
Accepted 3 November 2020
Available online 5 November 2020

Keywords:
Orthotropic steel decks
Residual stresses
Extended finite element method(XFEM)
Fatigue crack propagation

ABSTRACT

Orthotropic steel decks (OSD's) are susceptible to fatigue failure due to cyclic loading. Often fatigue cracks are found in the joint between the deck plate and the trough. Due to the welding process, residual stresses are present in and around the joint. In this paper, the effect of residual stresses on the fatigue crack propagation rate has been evaluated. First, a FE model has been made to predict and validate the residual stress field of the OSD due to welding. The validation of residual stresses is made comparing measured data at the surface of the OSD and over the thickness of the deck flange. The residual stresses are used to subsequently model for a crack propagation analysis based on extended finite element method (XFEM). The fatigue crack simulation including residual stress field shows good correlation compared to the experimental data, while the simulation without residual stress field shows less correlation. The effects of the residual stresses are relatively large as the tensile transversal residual stresses increase the crack propagation, while the tensile longitudinal residual stresses decrease the crack propagation rate. The optimal modelling of the component of residual stresses is investigated.

1. Introduction

Orthotropic steel decks (OSD's) are one of most common deck systems in steel bridges construction. Over past decades, OSD's shows sensitivity to cracks due to heavy traffic cyclic loads [1]. The fatigue life of OSD's is described in two phases namely fatigue crack initiation and fatigue crack propagation [2,3]. Due to welding defects and tensile residual stresses, fatigue cracks often occur around the welded connections within the orthotropic steel deck. Fig. 1 shows possible rib-to-deck crack positions [4]. The "Type II" fatigue crack propagation is mainly discussed in this paper.

---

* Corresponding author.
E-mail address: H.Xin@tudelft.nl (H. Xin).

https://doi.org/10.1016/j.matdes.2020.109294

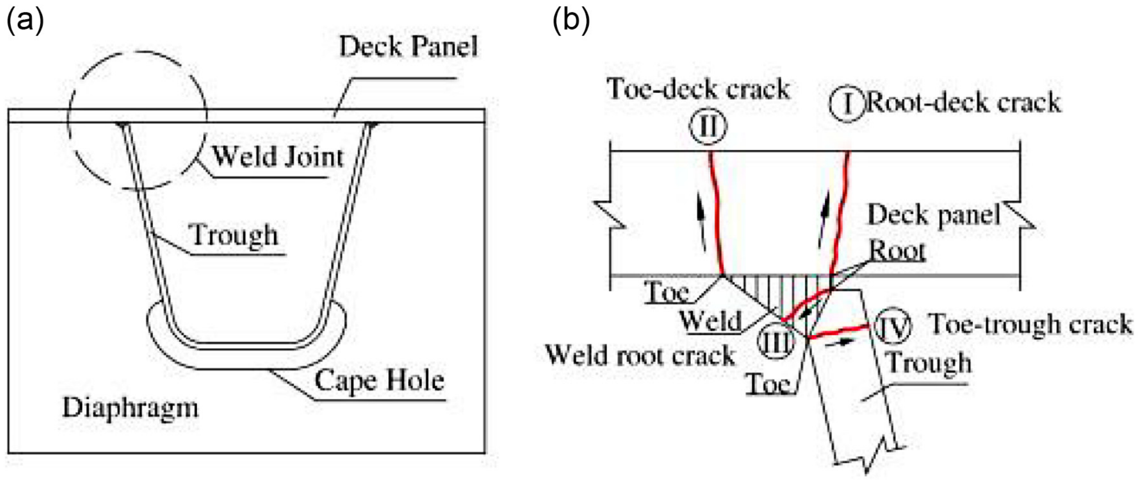

Fig. 1. Rib-to-deck joint fatigue cracks [4].

Residual stresses are internal stresses that exist in the OSD due to the shrinkage of the weld during the fabrication welding process. In welding, they arise due to the inhomogeneous temperature field generated during the process [5,6], localized restrained expansion and contraction in combination with local plastic deformation. Due to the restrained shrinkage of the heated material by surrounded cooler material, tensile residual stresses are formed at the vicinity of the weld. These stresses are equilibrated by compressive residual stresses, away from the weld area. Under external cyclic loading, tensile residual stresses can reduce the fatigue life by increasing the crack propagation rate. Compressive stresses are favourable in terms of fatigue life since they slow down the crack growth [7,8]. However, in the case of orthotropic steel decks, cracks have been observed in regions where the stress field due to external loads is nominally in compression. Therefore, it is expected that numerical models of orthotropic steel decks under cyclic loading overestimate the fatigue life without residual stresses [9]. Such observations have increased concerns about residual stress effects on fatigue crack initiation and propagation [2,10].

The residual stresses induced by welding process have a significant impact on both fatigue crack initiation and fatigue crack propagation of OSD's. The authors [11] investigated the residual stress on fatigue crack initiation of butt-welded plates made of high strength steels. The results showed that the residual stress influence the fatigue crack initiation position and the fatigue behaviour of butt-welded plate. FE-models numerically defined residual stress show better agreement with experimental results than the residual stress-free model. Teng et al. [12] evaluated the residual stress effect on the fatigue lifetime of the butt-welded plates based on thermal elastic-plastic analysis and strain-life method. Dong et al. [13]assessed the residual stress effect on fatigue crack initiation of the fillet welds after ultrasonic impact treatment based on the local strain approach. Chiffon et al. [14] analysed the influence of residual stresses on the fatigue crack growth on a weld toe geometry. The residual stress field of a cruciform welded joint is determined using X-ray diffraction and a finite element crack growth simulation using the J-integral and EPFM is performed and compared with experimental data. The results show that compressive stresses results in more favourable fatigue life, while a tensile residual stress field is unfavourable for the fatigue life. Taheri et al. [15] showed that the residual stress field due to the welding will change when the fatigue crack propagates trough the specimen. Acevedo and Nussbaum [16] investigated the influence of welding residual stresses on stable crack growth in tubular K-joints under compressive fatigue loadings. According to experimental results, fatigue cracks grow in compressive zones due to tensile residual stresses due to the welding process. The residual stress field has been measured using incremental hole-drilling method, X-ray diffraction and neutron diffraction. In addition, an uncoupled thermo-mechanical analysis is performed using Abaqus in order to obtain the residual stress field numerically. LEFM model derived from Paris law was developed on a compressive K-joint in order to estimate the effective stress intensity factor. This model shows agreement to the experimental measurements. It is shown that the tensile residual stresses have large influence on the fatigue crack growth.

In this study, a thermo-mechanical FE-analysis is conducted to obtain the residual stress field of an OSD-specimen. Based on the FEA, simplified residual stress filed assuming stress components in three directions, is proposed. These stress components are used as input in evaluating the residual stress effects on the fatigue crack propagation of OSD's. A crack propagation model of OSD-specimen based on extended finite element method (XFEM) is established, and the effect of the residual stresses on fatigue crack propagation is quantified.

2. FE-analysis of the welding process

In this chapter, the weld simulation analysis is made to obtain the residual stresses that are caused by the welding between the trough and the deck plate. The modelling of the welding process is separated in two phases. In the first part a thermal model is built, in which the heat transfer of the welding arc to the specimen is modelled using Finite Element Analysis (FEA). In the second part the stresses caused by the temperature change are modelled. These stresses are caused by restrained deformation due to expansion and shrinkage of the elements in the specimen. At the end of the simulation the residual stress field can be used in the fracture mechanics model. For additional details related to the welding simulation in the paper can refer to [6].

2.1. Thermal analysis

2.1.1. Geometry of the model

The OSD-specimen used in this research is taken from the research of W. Nagy [17], which is shown in Fig. 2. The specimen has a depth of 400 mm. The specimen is supported by two supports at either side of the through. At the left-hand side, the specimen is supported by a clamped support with a width of 40 mm (x-direction). At the right-hand side, the specimen is supported with a pinned support placed 50 mm away from the edge of the specimen. The deck has a thickness of 15 mm, while the trough has a thickness of 6 mm. There will be no mechanical load present on the specimen during the weld simulation model.

The specimens are welded using an automated welding process. The exact geometry of the weld of the OSD is not described in the report of

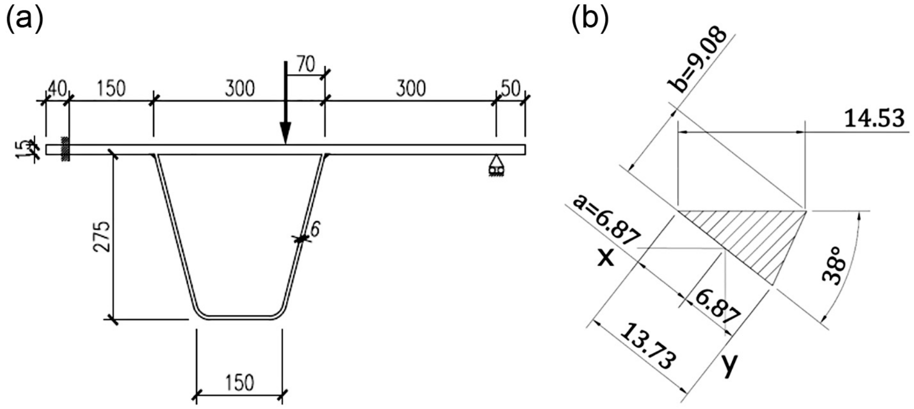

Fig. 2. a) Geometry OSD-specimen [17] b) Weld geometry.

W. Nagy. Therefore the final weld geometry in the FE model is simplified as shown in Fig. 2b. It is assumed that there are no imperfections in the weld and the weld is fully penetrated, which can lead to higher load cycles due to the lack of imperfections considered.

2.1.2. Material properties

The temperature dependent material properties refers to the NEN-EN 1993-1-2 [18]. Submerged Arc Welding (SAW) with Fluxocord 31 HD filler-material has been used for welding the OSD-specimens. According to the manufacturer [19], the filler material has a yield stress of $>420\ N/mm^2$ and a tensile strength of $500-600 N/mm^2$, which is both higher compared to standard S355 steel. However, it is assumed that there is no difference between the filler and parent material. In the experiment, there could be a difference depending on the welding conditions, filler material and imperfections. These differences are not taken into account in the FEM-analysis.

2.1.3. Element activation

In this paragraph, the 'birth and death' principle is further explained. At the beginning of the welding process, no weld material is present between the deck plate and the trough. The total weld has been divided in the FEM-model in 'weld segment' with a length of 10 mm. At the start of the analysis, no weld material should be present between the deck plate and the trough. However, before the analysis in Abaqus is able to start, the necessary weld elements were modelled. Therefore, in step 1, all the weld elements are deactivated using the command'Model change' in Abaqus to obtain the 'death' weld elements. After all the weld elements are deactivated, the thermal analysis can start. Every time step, one weld element is reactivated using the'Model change' command in the model. This process results in the 'birth' of the element. Simultaneously, the heat source model moves over the reactivated element. This simultaneous process simulates the heat input of the arc and the depositing of weld material to the OSD-specimen.

2.1.4. Heat input model

In the welding simulation model, the temperature of the specimen during the welding process will be modelled using the transient thermal analysis within Abaqus. The thermal process can be divided into three parts: Heat input due to the welding arc, heat transfer through the specimen and heat loss to the environment. This process is graphically shown in Fig. 3. The governing equation of the heat model is represented by Eq. (1).

$$c\rho\frac{\vartheta T}{\vartheta t}=k\left(\frac{\vartheta^2 T}{\vartheta x^2}\right)+k\left(\frac{\vartheta^2 T}{\vartheta y^2}\right)+k\left(\frac{\vartheta^2 T}{\vartheta z^2}\right)+q \tag{1}$$

where T is the temperature, t is the time, ρ is the density, c is the specific heat capacity, q is the internal heat generation rate and k is the thermal conductivity.

The heat flux is modelled using a DFLUX subroutine within Abaqus. With the subroutine, the heat energy input, caused by the welding, can be specified by magnitude, time and location within the model. Within the subroutine, the heat flux is calculated using two formulas and the specified weld parameters based on Goldak model [20]. This model consist of two ellipsoidal shapes, shown in Fig. 4, in which the heat flux by the welding is modelled. The heat flux is modelled by two power density distributions. The front power density distribution is shown in Eq. (2):

$$q_f(x,y,z)=\frac{6\sqrt{3}f_f Q}{abc_f\pi\sqrt{\pi}}e^{-3x^2/a^2}e^{-3y^2/b^2}e^{-3z^2/c_f^2} \tag{2}$$

while the rear power density distribution is shown in Eq. (3).

$$q_f(x,y,z)=\frac{6\sqrt{3}f_r Q}{abc_r\pi\sqrt{\pi}}e^{-3x^2/a^2}e^{-3y^2/b^2}e^{-3z^2/c_r^2} \tag{3}$$

All parameters used in both formulas are shown in Tables 1 and 2. In both equations Q is the power output of the welding machine. Within the subroutine, the Q is specified by multiplying the current A, Voltage V and the efficiency parameter. These parameters are taken from the report of W. Nagy [17]. First, the through and deck plate were connected using a few tack welds. Submerged Arc Welding (SAW) has been used for welding of the OSD-specimens. For the SAW welding an automatic single wire welding machine has been used. The specimen was first welded on one side, and then back from the other side of the trough. Parameters a, b, c_f, c_r, f_f and f_r define the geometry and magnitude of the heat source model and are shown in Table 2. These parameters are based on the geometry of the weld and on experimental data [20].

The x, y and z parameters determine the position of the heat source in the FEM-model. The origin of the heat model, shown in Fig. 4, the FEM-model is shown in Fig. 2b. Every second the heat source model moves 10 mm in negative z-direction. After 40 s, the right side of the specimen, with a length of 400 mm, has been virtually 'welded'. After the heat source model has passed the first side of the OSD-specimen, a short cooling period of 100 s is analysed by the FEM-model. The cooling period is needed to move the welding machine to the other side of the specimen. After the first cooling period the specimen is welded in the next 40 s. At last, a longer second cooling of 4000 s is applied, in order

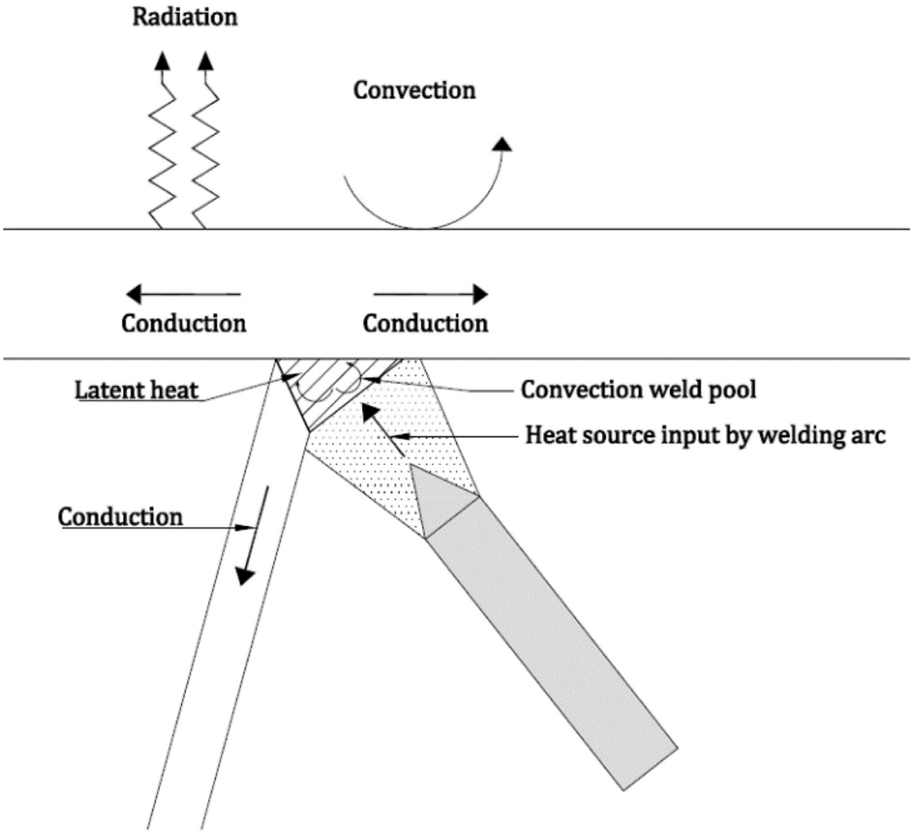

Fig. 3. Thermal process.

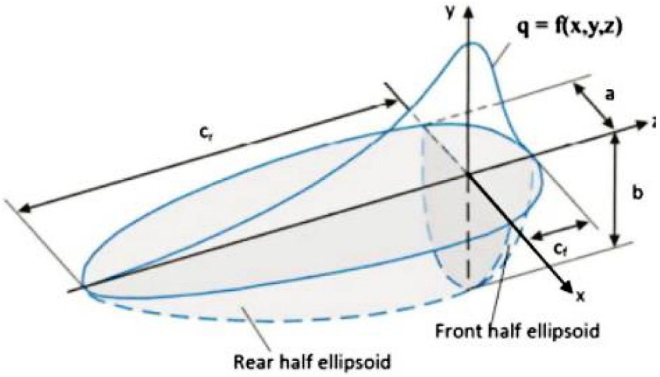

Fig. 4. Heat source model [20].

to let the specimen cool down completely. After these 4000 s the temperature field date analysis is completed.

2.1.5. Results of welding simulation

The results of the thermal model are temperature field data at every time step over the whole FEM-model. In Fig. 5, the molten zone of the weld in the OSD-specimen is shown. The boundaries of the HAZ of the experiment in the research of W. Nagy [17] can be compared with the thermal analysis. It is assumed that the steel used in the experiment melts around 1200°C. The contour plot of the weld area at $z = -200mm$, where temperatures ≥1200°C are denoted in light grey, is shown in Fig. 5. A comparison between the two models is shown in Fig. 5-c. Overall, the shape of the HAZ is similar compared to the experiment. The lack of imperfections in the FEA could lead to different results, especially around the weld root as lack of penetration is ignored.

Table 1
Parameters of welding process [17].

Welding Speed	10	*mm/sec*
Current	*26*	*A*
Voltage	*600*	*V*
Efficiency	*0.95*	
Heat flux	$1.48 * 10^7$	mW/mm^2

2.2. Mechanical analysis

The residual stresses are obtained in a mechanical FEM-analysis. The temperature field data is used as predefined field input during the analysis. During the mechanical analysis, the time steps as in the thermal model are applied. The stresses are obtained using the temperature depended material properties described in section 2.1.2. During the mechanical analysis, the material expands and shrinks due to the changes in temperature. During this variation in volume, stresses are generated due to restrained deformation. At the end of the mechanical analysis, the residual stresses are obtained due to the welding of the OSD-specimen.

In the mechanical and thermal analysis a number of assumptions have been made in order to simulate the welding conditions of the experiment. These assumptions might influence the results in some extend. All assumptions are listed below.

- The parent material and the filler material properties are the same according to the NEN-EN 1993-1-2 [18]. In real situation, the filler materail mechanical properties and properties around the heat effected zone differ. This influence the local behaviour creating uncertainties in estimating the life time predition of the initial crack. The temperature-depended material properties of the FEM-model are constant over the whole specimen.

Table 2
Geometric properties.

Width a	6.87	*mm*
Depth b	9.08	*mm*
Front c_f	6.87	*mm*
Back c_r	16	*mm*
Heat front f_f	0.6	
Heat back f_r	1.4	

- No material, geometrical and weld imperfections are modelled. Geometric imperfections consist of a slightly curved deck plate or variations in the thickness of the specimen. The weld imperfections such as a lack of penetration and slag inclusion are ignored. The mechanical analysis does not result in a constant residual stress field over the cross-section due to the boundary conditions and thermal expansion. Therefore, the cross-section at $z = -380$ mm, which is verified with the experimental data, is assumed to be present over the whole cross-section in the fatigue crack propagation analysis.

2.2.1. Boundary conditions

During the mechanical analysis, the mechanical boundary conditions of the OSD-specimen influence the stress distribution greatly. However, there is little information on the boundary conditions during the welding process. Our assumptions are based on the photo shown in Fig. 6. Assumed that all four edges of OSD-specimen are prevented to expand due to the increased temperature will lead to higher residual stresses due to additional restrained deformation. There are no rotational restrictions applied to the specimen. The supports are applied in each direction in order to keep the specimen in the correct position when the elements are activated step by step over time, during the 'birth and death' process. The boundary conditions in each of the three directions are shown in Fig. 6. At $z = -400$ mm, the OSD-specimen is supported in the z-direction. While at the right side of the specimen, the specimen is supported in the x-direction. First the tack welds are simulated in the FEM model. During the production of the specimen, a number of tack welds are placed in order to keep the trough and deck connected. These tack welds are modelled by not deactivating the welds at each corner at the first step. This ensures that the trough and deck cannot displace from each other. Also, at each corner the deck plate is supported in the y-direction in order to prevent that the OSD-specimen shifts up and down due to the internal stresses. The results are compared with experimental data in paragraph 3.2.3.

2.2.2. Results

Due to the heat introduced into the mechanical model, the specimen was expanded. In the manufacturing process, the OSD-specimen was in unrestrained conditions in both x- and y-direction. As the free edges can deform freely, the residual stresses at these edges is very low, while at the restrained edges the residual stresses are very high. This phenomenon is shown in Fig. 7 with the red arrow, where at the right upper corner the residual stresses will be relatively high and at left lower corner relatively low.

Therefore, it is important to evaluate at which cross-section the residual stresses correspond with the experimental data. The residual stresses of this cross-section will be assumed constant over the whole cross-section during the fatigue crack simulation. As it can be seen in Fig. 6, a section of 4000 mm is welded, wherefrom OSD-specimens of 400 mm are cut. In this way, the OSD-specimens in the middle section

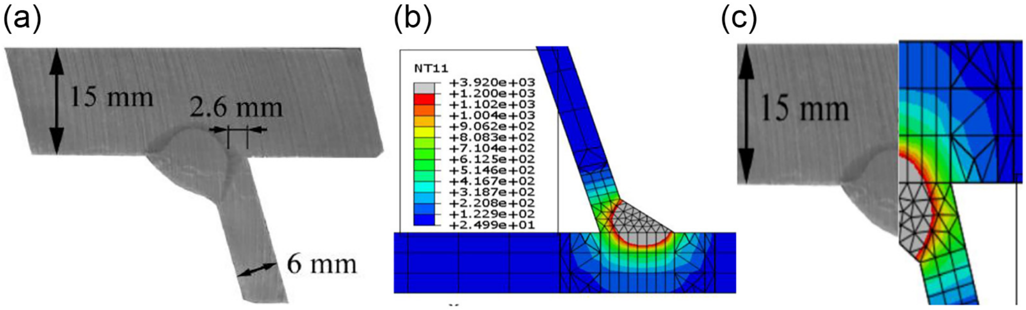

Fig. 5. Comparison between experiment and FEM-model [17,21].

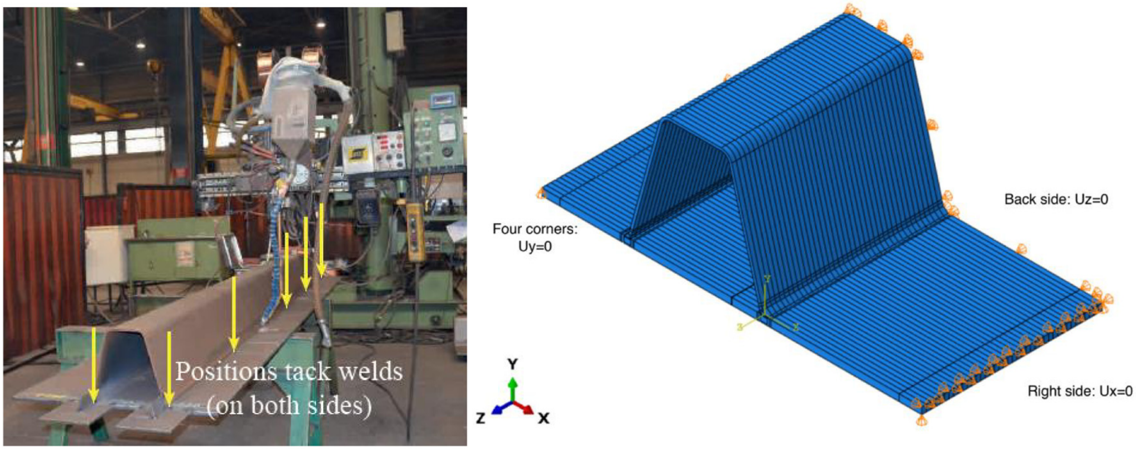

Fig. 6. Overview welding process [17] & boundary conditions.

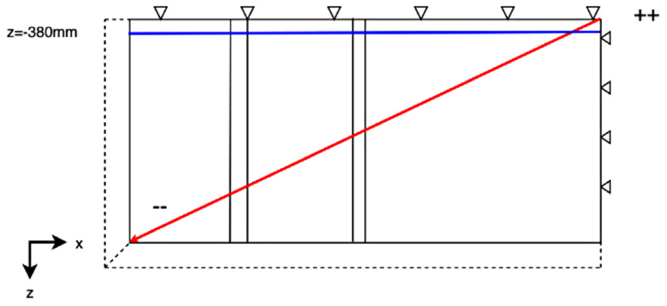

Fig. 7. Thermal expansion mechanical model.

have a nearly constant residual stress distribution over the cross-section of the weld. This justifies the method of using a cross-section of the residual stress field over the whole length of the OSD-specimen in the fatigue crack propagation simulation, as the residual stress field will be constant over the whole width (z-axis) of the specimen. The cross-section chosen is along the blue line at z = -380 mm, as the stresses at this position correspond with the experimental data described in the next paragraph. In Figs. 8-10, the stresses of the FEA are displayed using contour plots.

Based on the numerical results of the mechanical model, a simplification of the stresses in each direction is made. After the mechanical analysis, the contour plots of the stresses are analysed in steps of 10 MPa. After that, zones have been made of the residual stress field in the global axis system. The simplified residual stresses are shown in Figs. 8-10. The stresses are shown in the global axis system, so residual stress component S11 are in the x-direction, residual stress component S22 in the y-direction and residual stress component S33 in the z-direction. As can been seen in the simplification of residual stress components S11 and S33, the stresses are not symmetrical. This is due to the asymmetrical geometry and the sequential weld sequence. The simplified stresses will be used in the crack propagation model, where the influence of the stresses in each direction will be analysed.

2.2.3. Verification of results

The experimental data are obtained by Incremental Hole Drilling (IHD) measurements using Strain Gauge Rosettes (SGR). These SGRs are placed in two groups, denoted as left and right, on the outside of one trough. The position of the SGRs around the weld region is shown in Fig. 11. In Fig. 11, all the yield stress of the material is denoted with a thin green line. The transversal residual stresses are slightly lower compared to the experimental data at all three positions. However, the residual stresses in the longitudinal direction are around the yield strength (355 MPa) in the FEM-model, while the experimental results are much lower around the 250 MPa. In the report [17], it is stated that these stresses should be around the yield stress. The residual stress level is validated by welding simulation of another geometry described in Chapter 4 of the thesis [17]. The longitudinal stress in this analysis

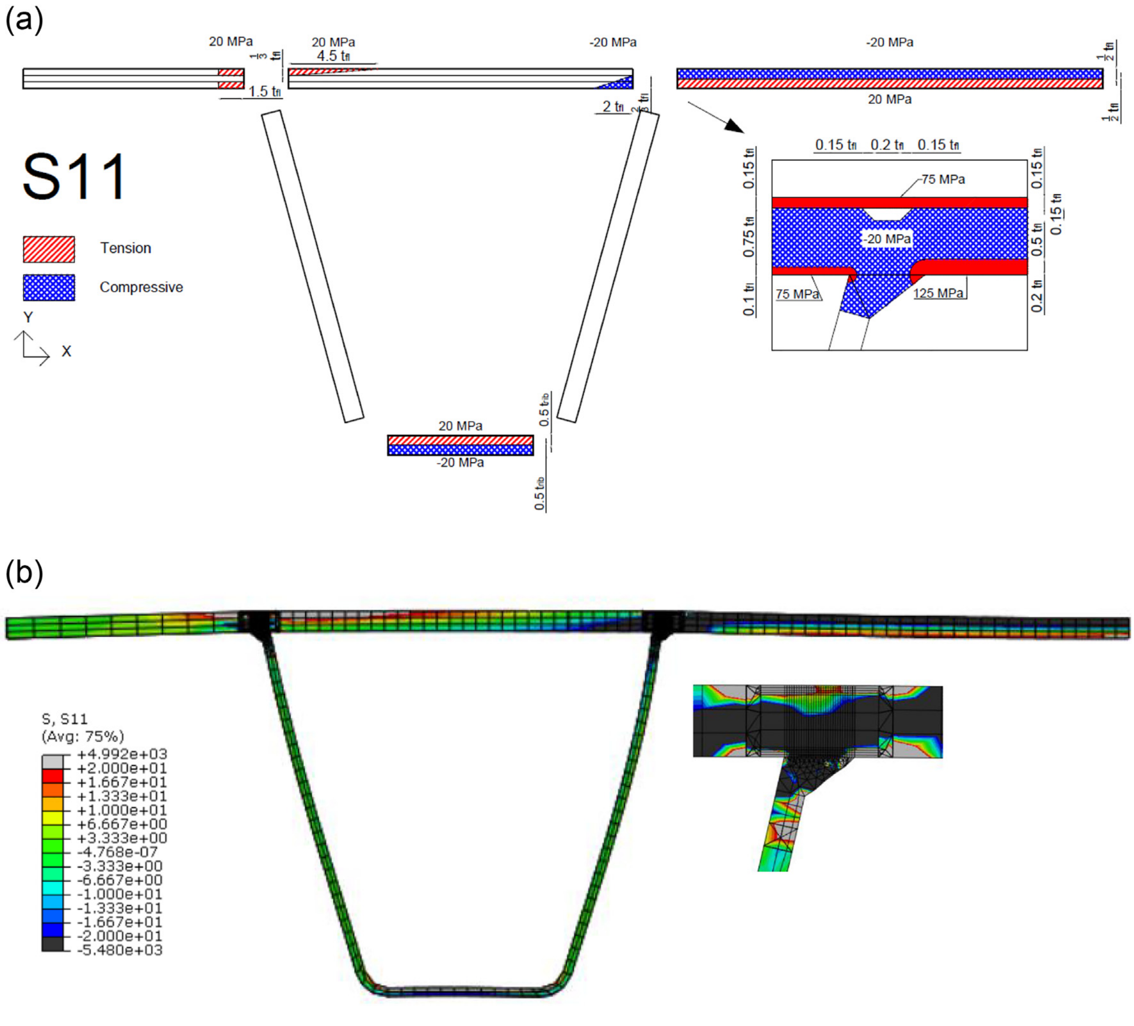

Fig. 8. a) Simplified residual stresses S11. b)FEA-output S11.

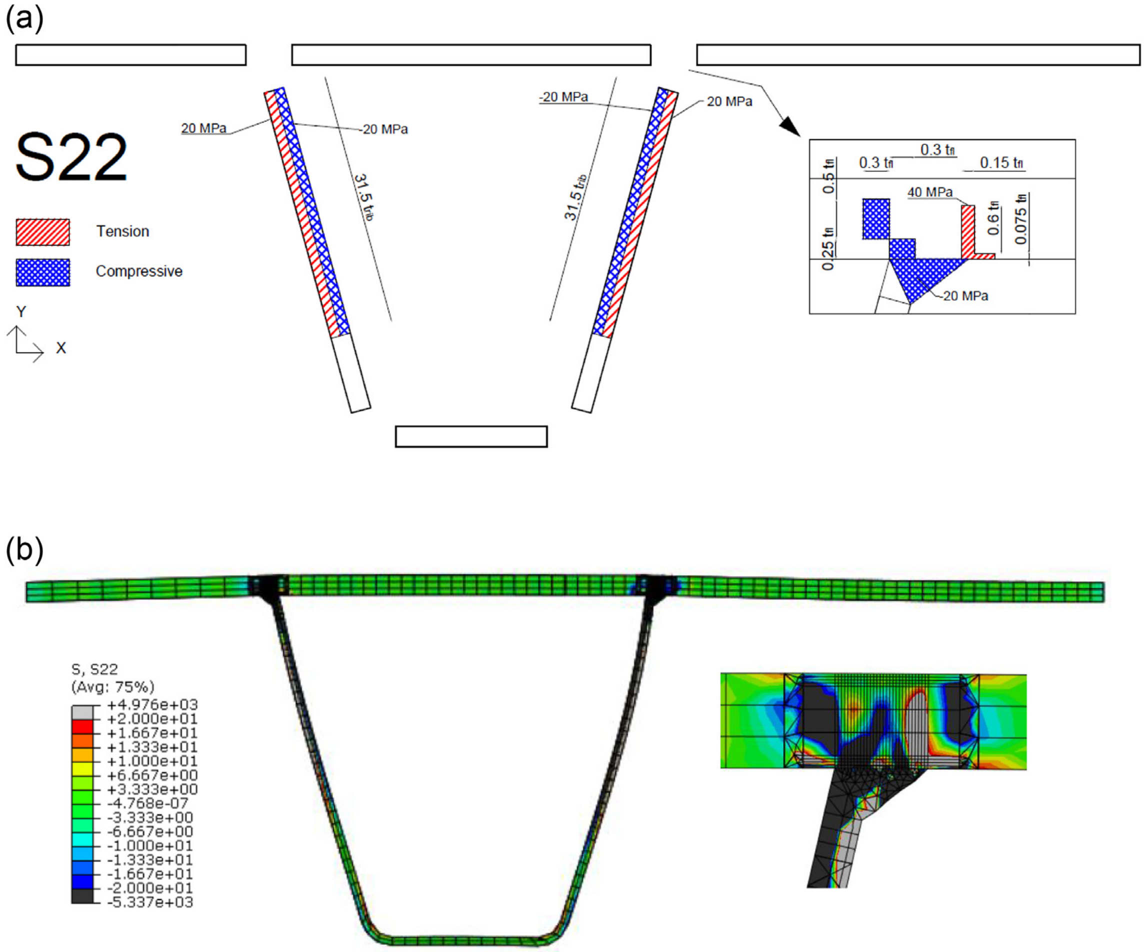

Fig. 9. a) Simplified residual stresses S22. b) FEA-output S22.

was around the yield strength in both the experiment and the FEM-model. The results of this analysis are shown in Fig. 12. The transversal residual stresses correspond well with the experimental data. While the residual stresses in the longitudinal direction are around 400 MPa, which is slightly higher than the yield stress. This position is of great importance as the initial crack will be placed there in the fracture model.

In Fig. 13, the results of the mechanical analysis are compared to other similar experimental data of Kainuma et al. [22]. In this research the transverse residual stresses along the thickness of the deck at the weld toe have been determined using both experimental data and FE-analysis. In this comparison, the FE-analysis performed in this report will be compared with both the FE and experimental results. As the thicknesses of the deck and stiffener of both the experimental data and the FEM-model are different compared to the geometry used in this report, the relative thickness of the deck is used to compare the results. The transverse residual stress data from the experimental data is obtained using strain gauges along the deck thickness, while the transverse residual stress data of the FE-analysis is obtained directly from the FEM-software used by Kainuma et al. [22]. From the results of the FEA, it can be seen that the mesh size in the middle of the deck is coarser compared to the top and bottom of the deck. The mesh on the top and bottom has a size of 0.5 mm in order to correctly compare with the experimental data of W. Nagy, while in the middle a mesh size of 3.67 mm is applied.

3. Fatigue crack simulation analysis

In the first part of this chapter, the FE model has been verified using measurements from a static experiment [15]. The fatigue crack simulation using XFEM has been described and verified using experimental data, in the second part of the chapter. Considering the material properties only elastic material properties, E-modulus = 210 GPa and $\nu = 0.3$ are applied for the parent and weld material in the static analysis.

3.1. Comparison FE results with the static test data

3.1.1. Geometry and boundary of the model

The test set-up and boundary conditions of FE model [17] are shown in Fig. 14a. The specimen is 400 mm long, in the z-direction. Supports are at both sides of the through perpendicular to the x-direction. A clamped support is 40 mm from the "left edge" of the specimen, and a pinned support is 50 mm from the "right edge" of the specimen. The deck thickness is 15 mm, while the trough has a thickness of 6 mm. At the deck, the top of the trapezoidal stiffener is 300 mm wide, while the width at the bottom is 150 mm. The stiffener height is 275 mm. A hydraulic jack is used to apply the load in force control, via a beam having a round edge. This results in a line load of the specimen at 420 mm from the right edge of the specimen. It should be noted that the initial imperfections of the OSD-specimen and possible uneven loading is not considered in FEA.

The boundary conditions strongly influence the stress distribution of the FE model. Therefore, it is important to model the boundary conditions as close as possible to the set-up, shown in Fig. 14a. The boundary conditions of the FEM-model are shown in Fig. 14b.

3.1.2. Loading

The line load positioned 70 mm from the weld toe, see Fig. 14b, is used in the static analysis to compare to the experimental results to

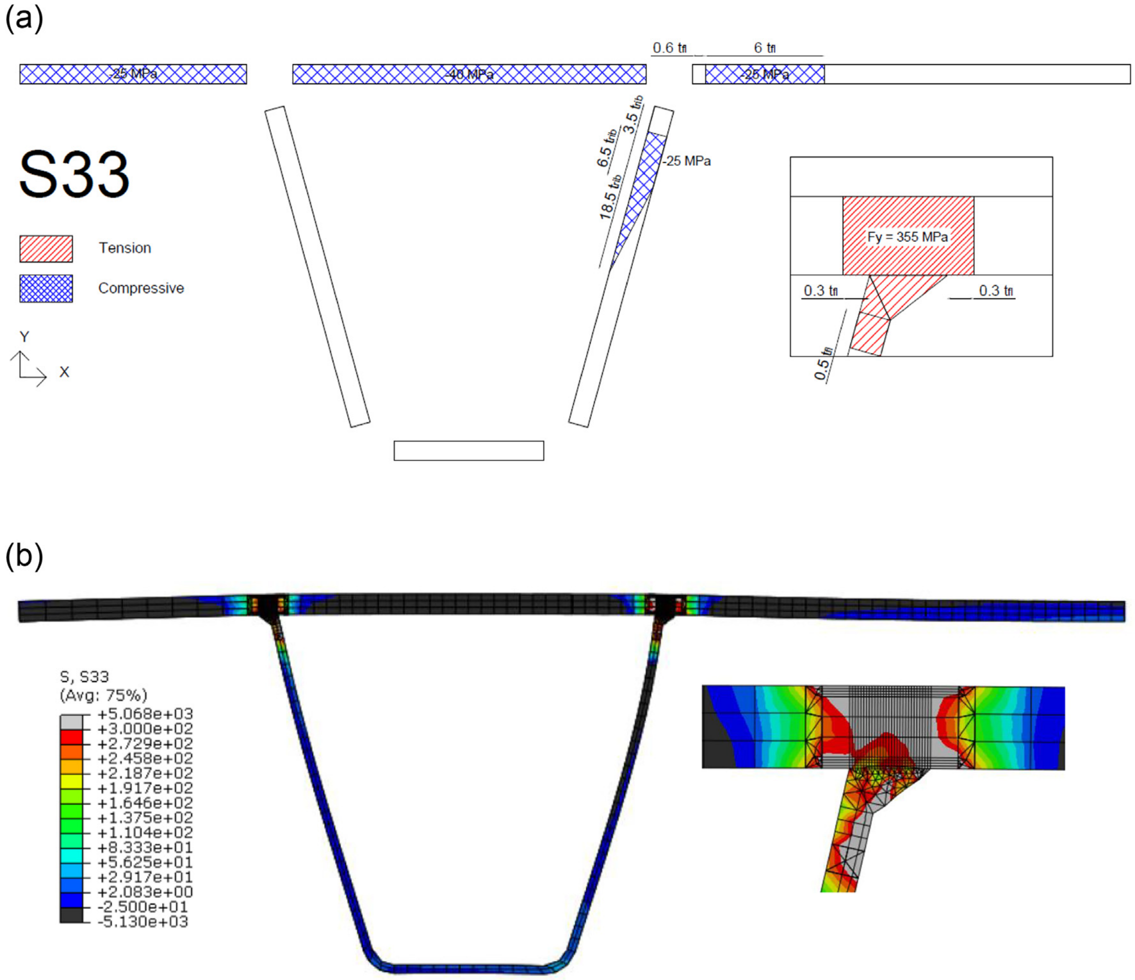

Fig. 10. a) Simplified residual stresses S33. b) FEA-output S33.

the FEA. Strain gauges are placed closed to weld to measure the strains. The displacement of the OSD-specimen is obtained at the point of loading from the displacement of hydraulic cylinder. These static experiments are done in the range +/— 40 kN.

3.1.3. Displacement

Displacement in the y-direction measured in the experiment is compared with the FE results in Fig. 15. The OSD-specimen is slightly stiffer compared to the experiment. This is due to the stiffness of the experimental set-up. This set-up deforms due to the loading leading to a bit larger displacement in the experiment compared to the FE-analysis.

3.1.4. Strain

The strain is analysed in the longitudinal direction (z-direction) of the OSD-specimen. The strains are analysed at sections 25 mm respectively from the weld toe and the weld root. Also, the strains are measured in the middle cross-section of the specimen. The comparison between the experimental data [17] and the FEM-model are shown in Figs. 16 and 17. It can be seen that the strains of the FE-analysis are lower compared to the experimental results. The influence of the boundary conditions can explain this. At the experimental setup, the boundaries are not infinitely stiff as in the FEM-model. Also, in the FEM-model the contact areas at support are not considered in FEA. The influence of these two effects are addressed in the recommendations.

3.1.5. Hot spot stresses

The stress is analysed in the transversal direction (x-direction) at the middle cross-section of the specimen, see Figs. 18 and 19. In both cases there is a singularity at either the weld root or the weld toe. The measurement position for evaluation of hot-spot stress is detailed in Fig. 20.

3.2. Fatigue crack propagation

A crack propagation analysis is performed using XFEM based on LEFM and VCCT (Virtual Crack Closure Technique). The results of the analysis are compared with the experimental data [17]. The residual stresses obtained by the weld simulation model in the previous section are included. FEA with the residual stresses and without residual stresses are considered to evaluate the influence of the residual stresses on the crack propagation. Influence of a residual stresses component in each direction is quantified below.

Assumptions are made in the fatigue crack propagation analysis. These assumptions might influence the results to some extend, as it is discussed below.

The boundary conditions are simplified because of the lack of experimental information.

The same assumption as in section 2.1.2 is used here. Mechanical properties of the parent material and the filler material are the same. The Paris law properties of the weld could be different compared to the parent material.

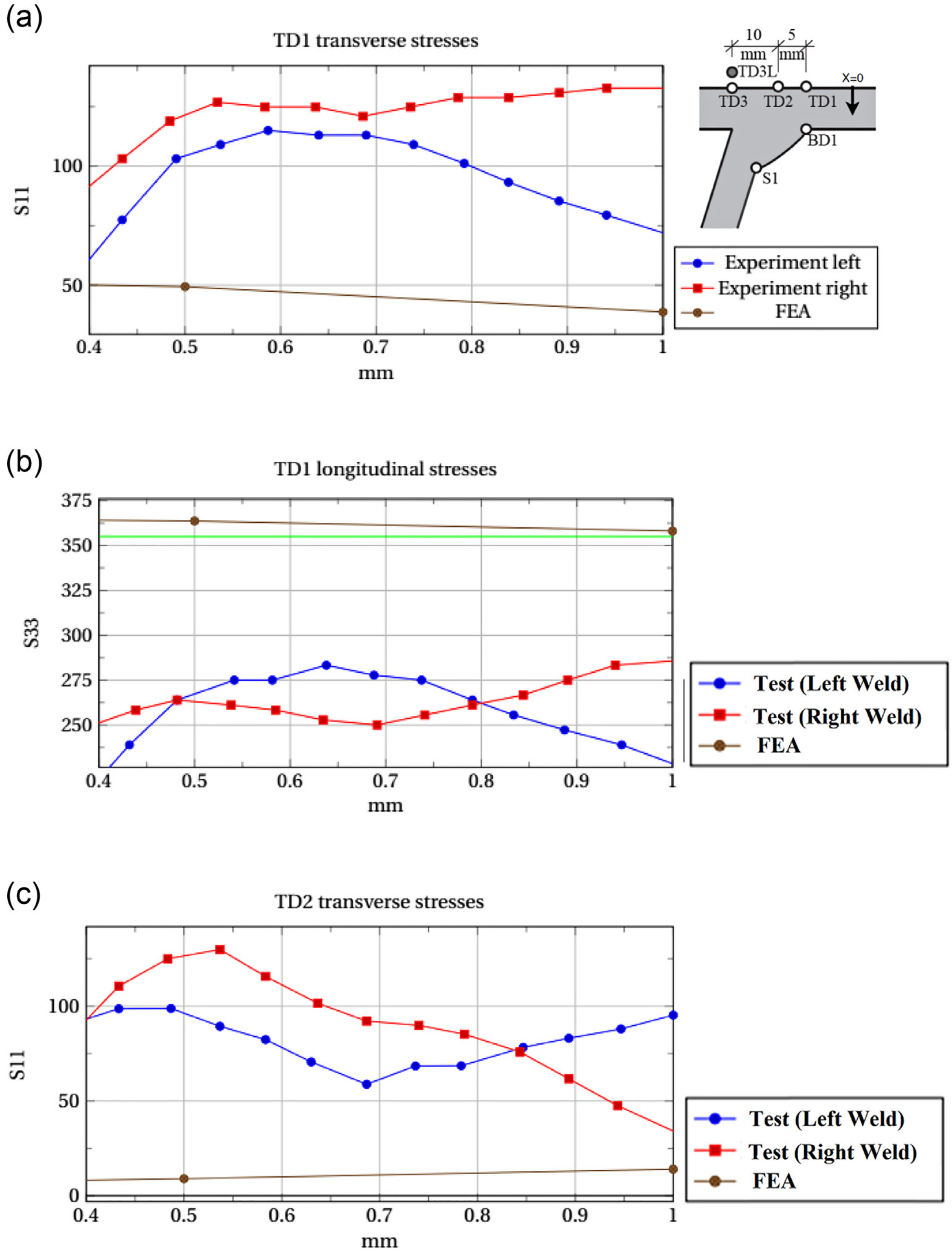

Fig. 11. Comparison of measurements of residual stress in positions of SGRs [17] with results of FEA.

Due to the different boundary conditions between the mechanical model and the crack propagation model, the inserted residual stresses are not in equilibrium in the fatigue crack propagation simulation. Possible small changes in the stress field could appear, because of this assumption.

3.2.1. Fatigue crack propagation model

The extended finite element method (XFEM) is used to model the fatigue crack propagation using commercial finite element software ABAQUS [23]. XFEM is used to ensure automatic crack propagation after an initial crack is included in the mesh. The mesh has to be sufficiently small because the smallest crack increment is equal to the length of the element side. VCCT is used for the crack propagation analysis based on LEFM in combination with a direct cyclic load. The Paris Law, shown in Eqs. 4 and 5, is used to formulate the fatigue crack growth propagation under cyclic loading.

The Paris formula, shown in Eq. (4), is expressed in terms of energy release rates and the crack propagation rate, as shown in Eq. (5). The direct cyclic loading module, as implemented in Abaqus, leads to the threshold shown in Eq. (6). The crack is growing when this criterion is satisfied. Usually constants c_1 and c_2 are set very low to immediate start the crack growth.

$$\frac{da}{dN} = C\Delta K^m \tag{4}$$

$$\frac{da}{dN} = c_1 \Delta G^{c_2} \tag{5}$$

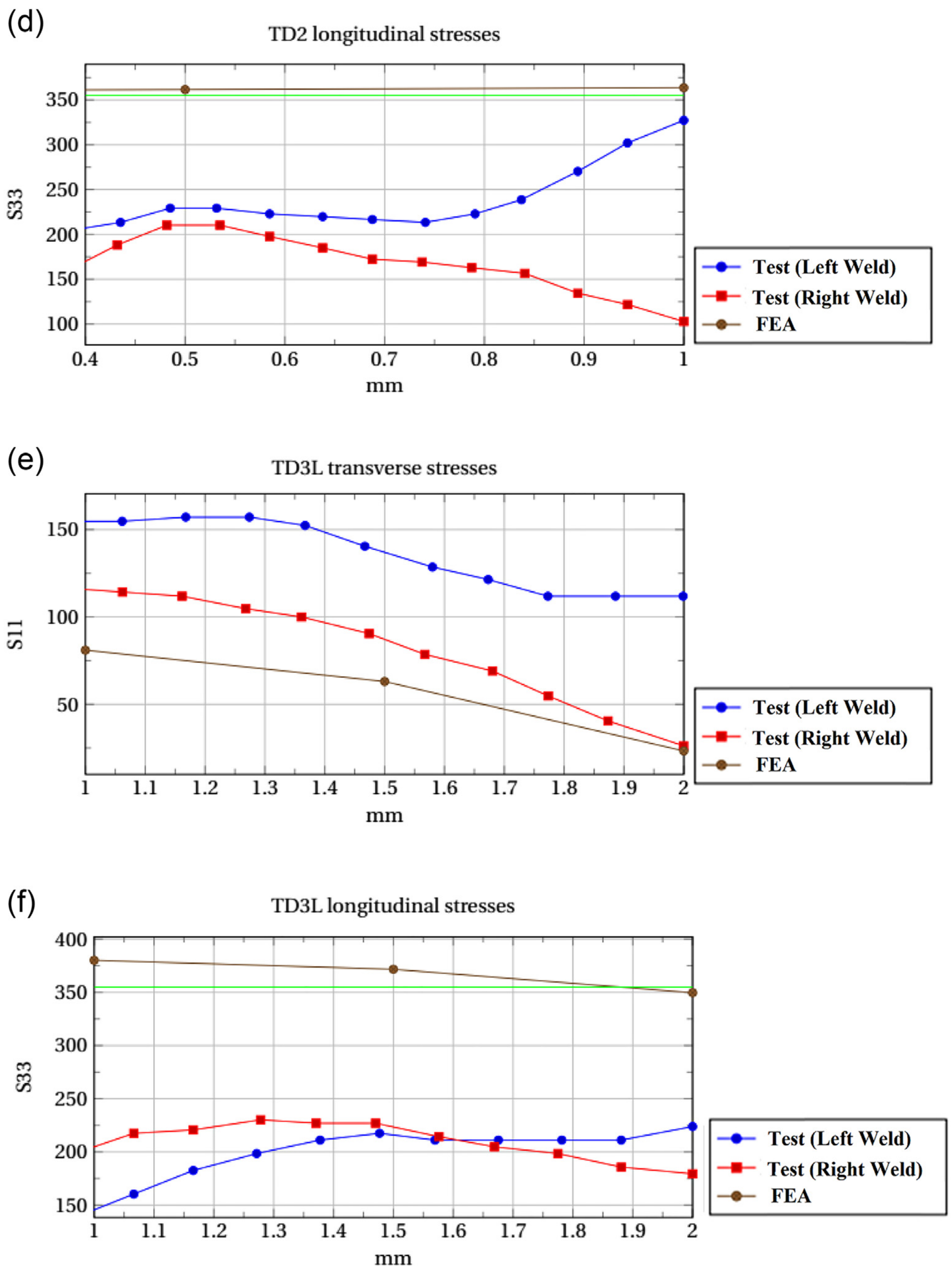

Fig. 11 (*continued*).

$$f = \frac{N}{c_1 \Delta G^{c_2}} \quad \geq 1.0 \tag{6}$$

Fatigue crack growth in the Paris regime is only possible when Eq. (7) is met. Then, the relative energy release rate is larger than G_{thresh} but less than G_{pl} to ensure the fatigue crack growth.

$$G_{thresh} < G_{max} < G_{pl} \tag{7}$$

The following parameters apply in the Paris law region. Both material constants need to be rewritten in terms of energy, see Eqs. (4), (8) and (9). The relative fracture energy release rate is ΔG, $E' = E$ for plane stress and $E\prime = \frac{E}{1-\nu^2}$ for the plane strain. Once the crack growth is started, Eq. (8) is used to model the stable crack growth. Using VCCT, the amount of energy to propagate the crack is computed. If the amount of energy is higher than G_{thresh}, the element will crack. The stable crack growth of the element will be calculated using Eq. (8) (Paris Law), in which the propagation direction, length (Δa) and amount of load cycles (N) are computed. After the element is cracked, the stress field is re-calculated and the next element that cracks is calculated based on VCCT and the Paris law. The element, in the enriched region, which requires the least amount of cycles, will be cracked first. This procedure is repeated which results that every step results in the propagation of one element at a certain number of load cycles.

$$\frac{da}{dN} = c_3 \Delta G^{c_4} \tag{8}$$

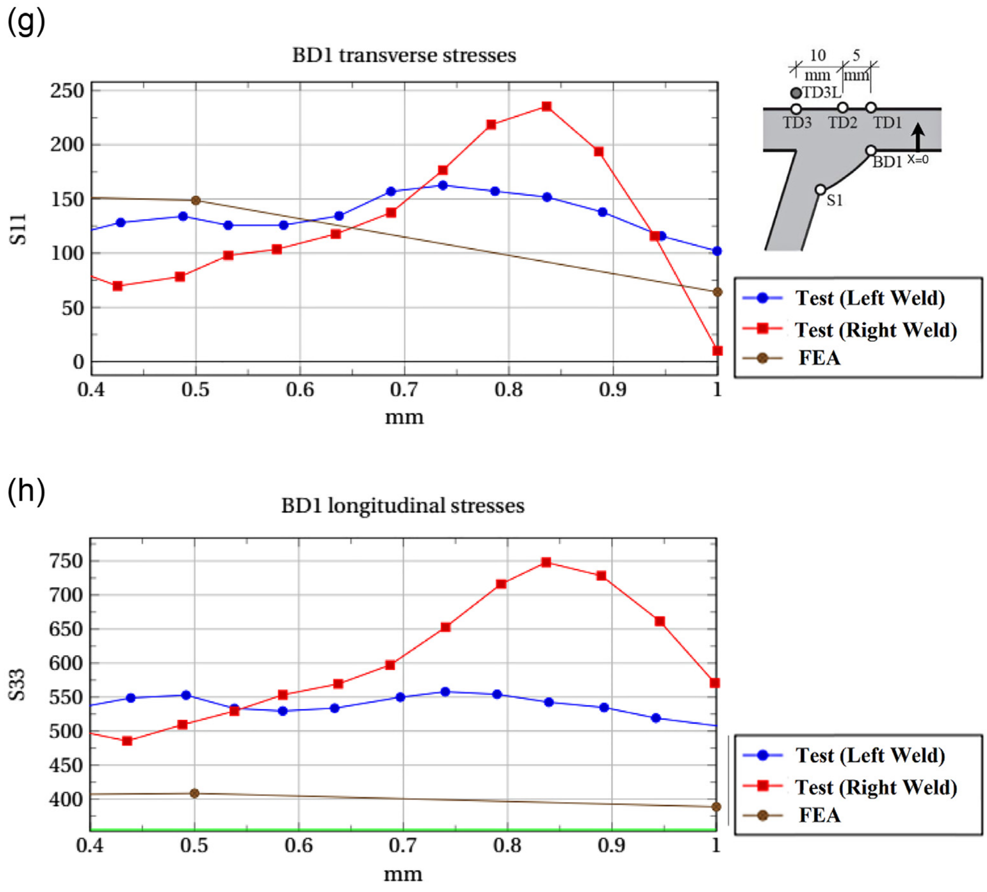

Fig. 11 (*continued*).

$$c_3 = CE'c_4 \qquad c_4 = \frac{m}{2} \tag{9}$$

The G_c can be specified using various mixed mode models within Abaqus. The Power law expressed by the Eq. (10) is used in this paper. The procedure of crack propagation used by based on a combination of Paris Law and VCCT is illustrated in Fig. 21. Using VCCT, the amount of energy to propagate the crack is computed. If the amount of energy is higher than G_thresh the element will crack. The stable crack growth of the element will be calculated using the Paris Law in which the propagation direction, crack length and amount of load cycles (N) are computed. After the element is cracked, the stress field is re-calculated and the next element that cracks is calculated based on VCCT and the Paris law. The element in the enriched region, which requires the least amount of cycles will be cracked first. This procedure is repeated which results that every step correspond with the propagation of one element at a certain number of load cycles.

$$\frac{G_{eq}}{G_{eqC}} = \left(\frac{G_I}{G_{IC}}\right)^{a_m} + \left(\frac{G_{II}}{G_{IIC}}\right)^{a_n} + \left(\frac{G_{III}}{G_{IIIC}}\right)^{a_o} \tag{10}$$

3.2.2. Geometry and boundaries of the FE mesh

The geometry and boundary conditions are the same as shown in 3.1. However, in the fatigue crack simulation an initial crack is inserted, to start the fatigue crack growth. The XFEM-model is compared to fatigue experiment [17]. The fatigue load accounting and the crack

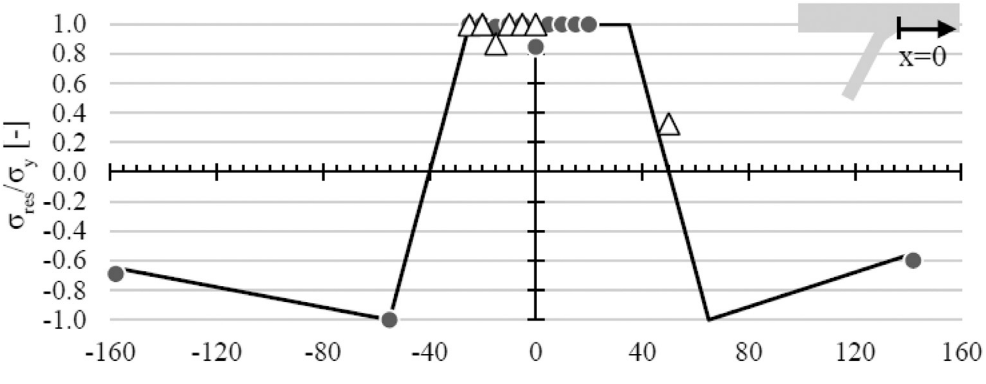

Fig. 12. Results chapter 4 longitudinal stresses top deck [17].

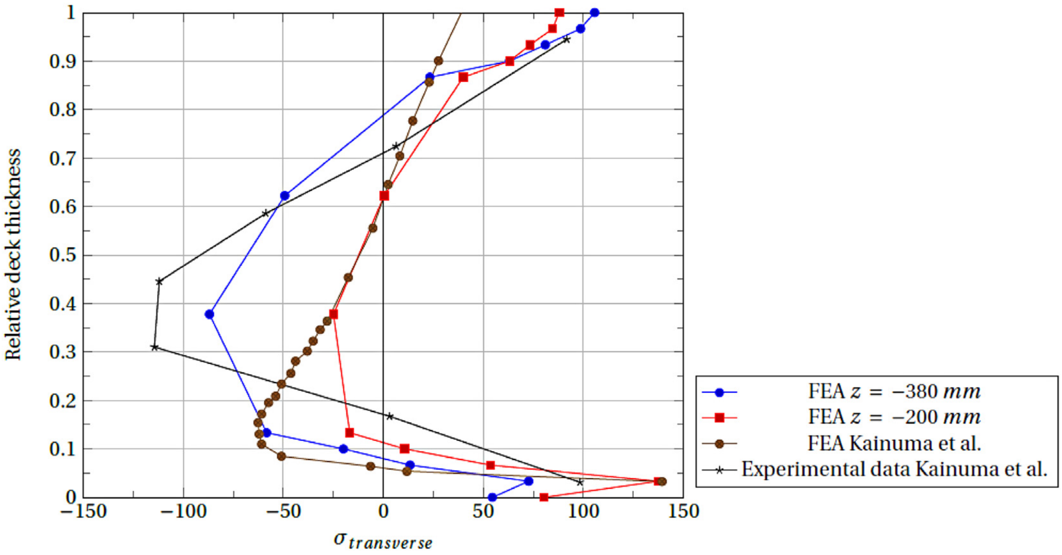

Fig. 13. Comparison between FEA results and literature data [22].

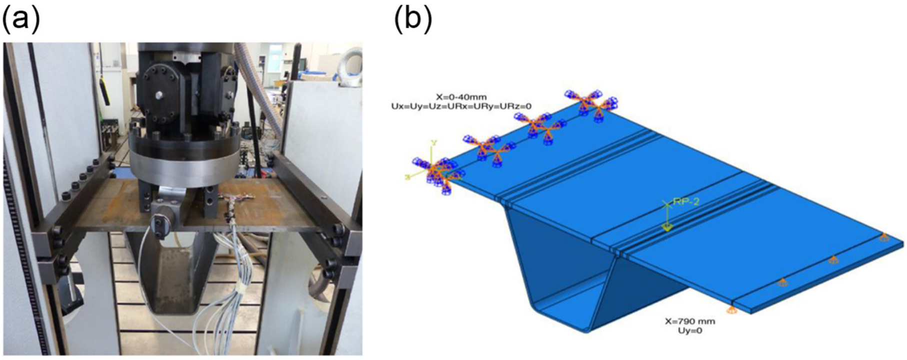

Fig. 14. a): Test setup OSD-specimen [17]. b): lay-out the FE model including boundary conditions.

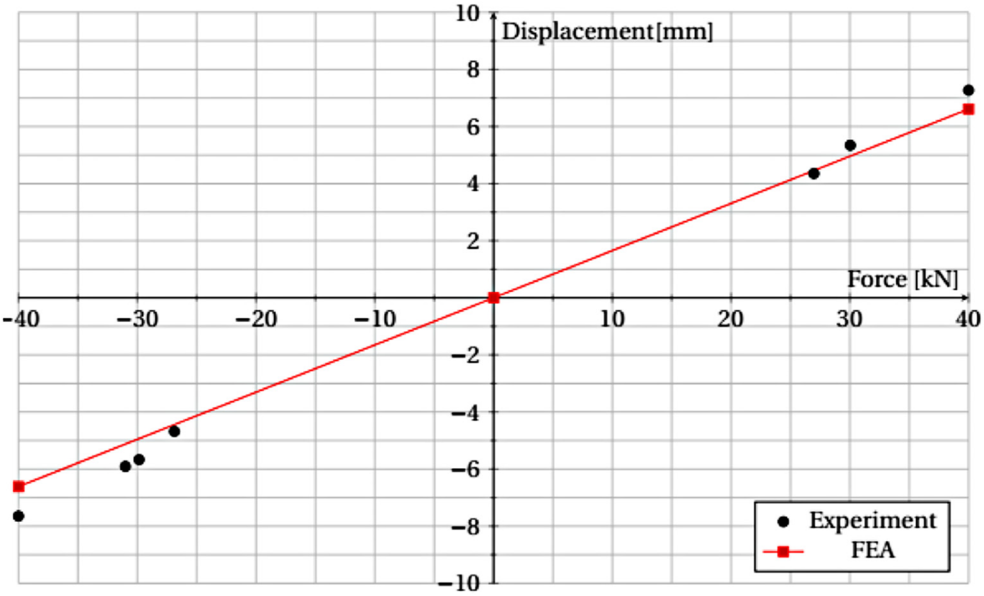

Fig. 15. Displacement in the y-direction [17] compared to FE results.

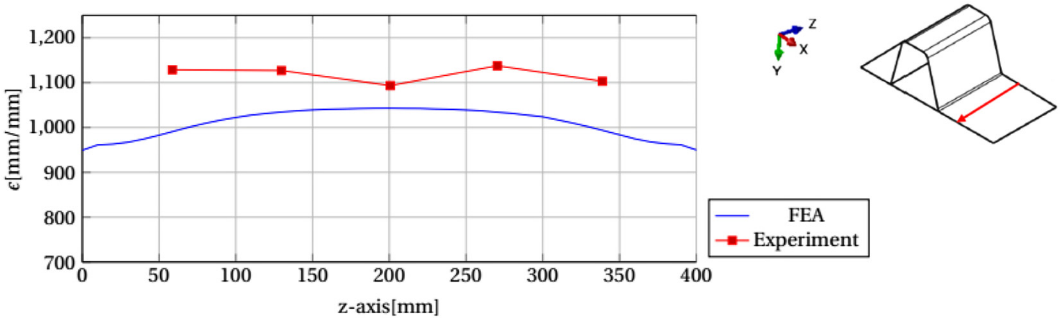

Fig. 16. Longitudinal strain in the deck [17].

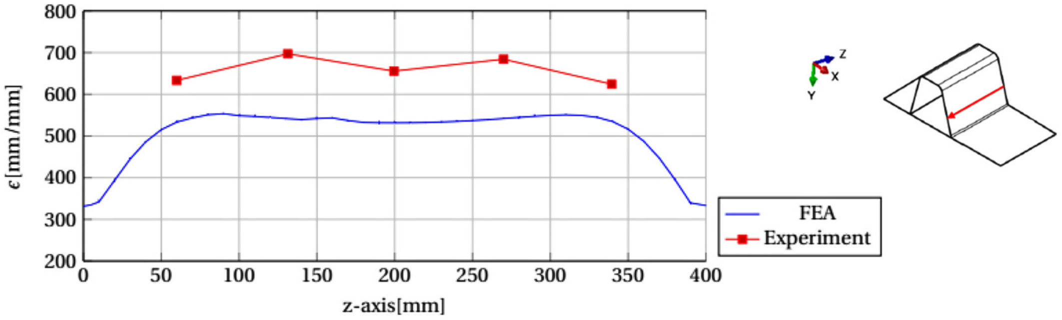

Fig. 17. Longitudinal strain in the trough [17].

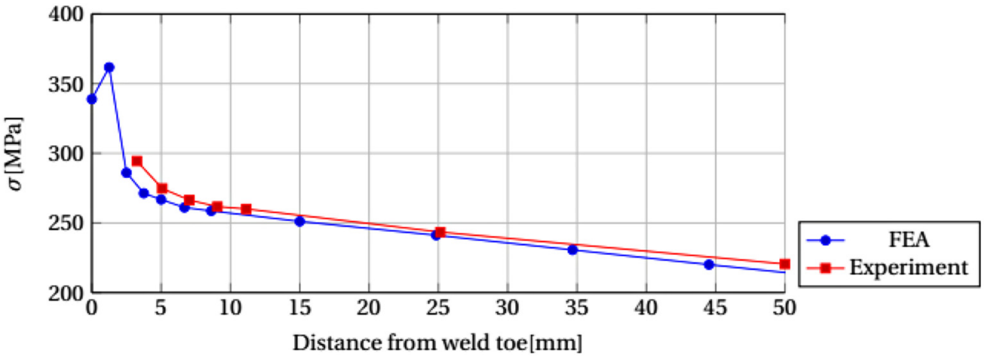

Fig. 18. Transversal stress in the x-direction in the deck, distance is from the weld toe [17] at the middle cross-section.

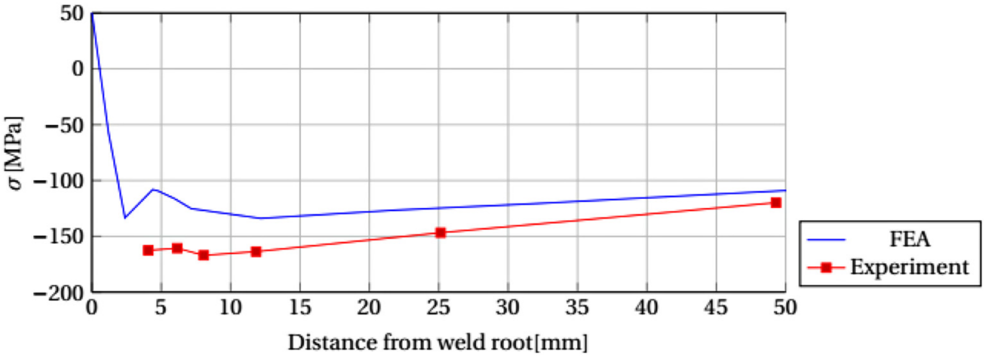

Fig. 19. Transversal stress in the x-direction in the trough, distance is from the weld root [17] at the middle cross-section.

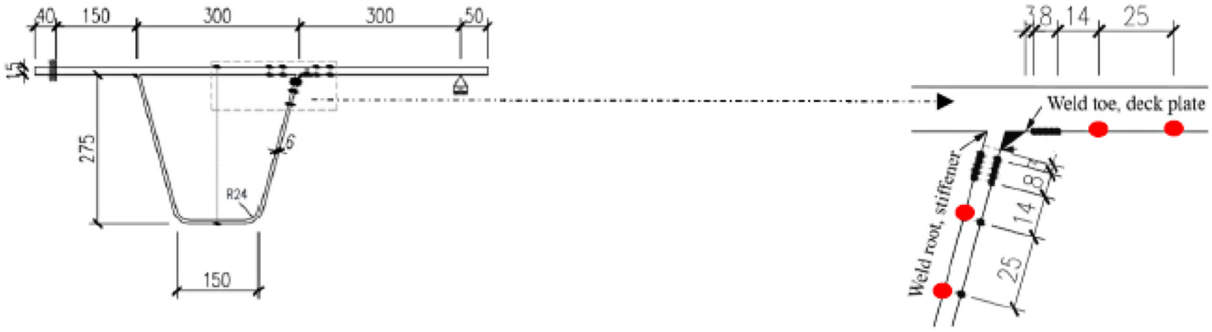

Fig. 20. Measurement positions for evaluation of the hot spot stresses [17].

propagation of an OSD-specimen were monitored. The initial crack size in depth of the deck plate, denoted as *a*, and the length of the crack, denoted as 2*c*, were measured using beach mark measurements and fractographic analysis. These experimental data are compared to results of the XFEM-model. The initial crack is placed in the middle of the OSD-specimen at the weld toe, see Fig. 22. The shape of the initial crack is rectangular, where the crack depth is denoted as *a*, the half-length of the crack is denoted as *c* and the total crack length is denoted as 2*c*. The rectangular shape is chosen to comply with used FE mesh. The initial crack size is based on experimental data of W. Nagy, see Fig. 22. The initial crack depth is around 1.5 mm and the total crack length is around 275 mm corresponding 170.000 cycles. The XFEM-model is used to simulate the crack increase from 1.5 mm until the failure. The crack initiation phase is not modelled as there are no experimental data available for this phase. Both graphs are based on beach mark measurements of specimen No. 10.

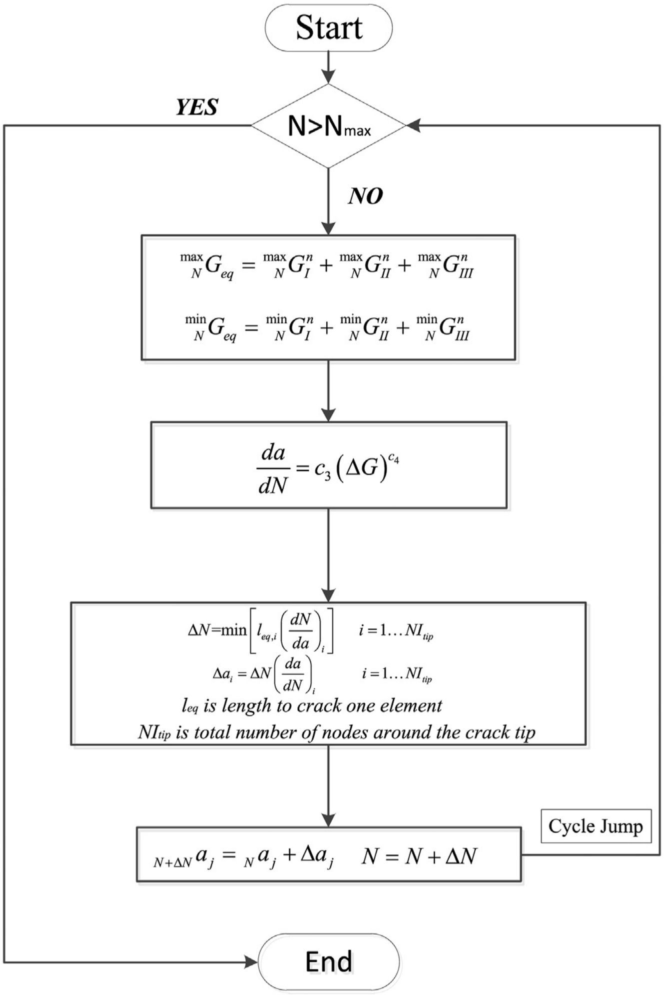

Fig. 21. Illustration of XFEM propagation progress (The threashold is not presented).

Influence of the residual stresses on the crack propagation is evaluated using the stresses due to the welding. The residual stresses are imported in Abaqus using the function 'Predefined Field'. Every stress component (S11, S22 and S33) introduced in each direction is analysed separately to quantify the effect of each component. The complete stresses field in all three directions is analysed as well.

The simplified residual stresses are imported into the fracture model. After the first static analysis, the stress field might change due to the different boundary conditions. The changes in the stress field can be small if the boundary conditions are similar. Also, due to the inserted stress and difference in boundary conditions, the OSD-specimen is deforming slightly due to the unbalanced stresses.

The mesh around the weld region is shown in Fig. 23b, with more refined mesh around the weld area. In the enriched region around the crack zone, linear hexahedron (C3D8) elements with a size of 0.75 mm are used. Between the refined and non-refined mesh, tetrahedron (C3D10) elements are used to establish transition in element type and size. For the rest of the non-refined mesh, linear hexahedron (C3D8R) elements are used with a global size of 10 mm.

3.2.3. Loading model

During the crack propagation analysis in Abaqus, a direct cyclic analysis is performed. The load is applied as a line loads, at the distance of 70 mm from the weld root. This quasi static analysis simulates cyclic loading based on a varying load. The varying load is modelled using a periodic function in order to mimic the loading test reported in [17]. The load of −31 kN is multiplied with a periodic function dependent of time in order to simulate cyclic loading. This periodic load, shown in Fig. 23a, is a function of time, where one load cycle coincides with one second in time.

3.2.4. Material properties

In this model, both elastic material properties and Paris Law properties are applied, E = 210 GPa and $\nu = 0.3$. The Paris law properties C_3 and C_4 are based on the literature data in [17], while the fracture toughness parameters are based on other literature [24] as these data are not specified in [17]. The Paris law parameters are shown in Table 3.

3.2.5. FE results and crack propagation in the experiment

The results of the FEA with and without residual stresses are shown in Figs. 24 - 26. Each residual stress component, S11, S22 and S33, corresponding to the residual stresses in x-, y- and z-direction, are introduced into the XFEM-model separately to obtain the effects of each residual stress component.

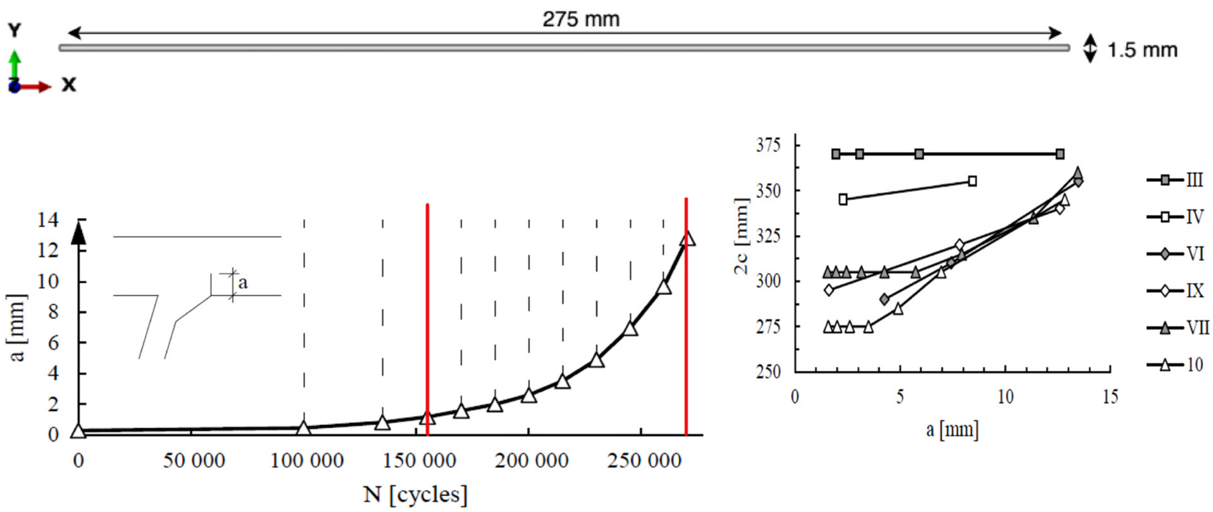

Fig. 22. Initial crack and depth Specimen 10 [17].

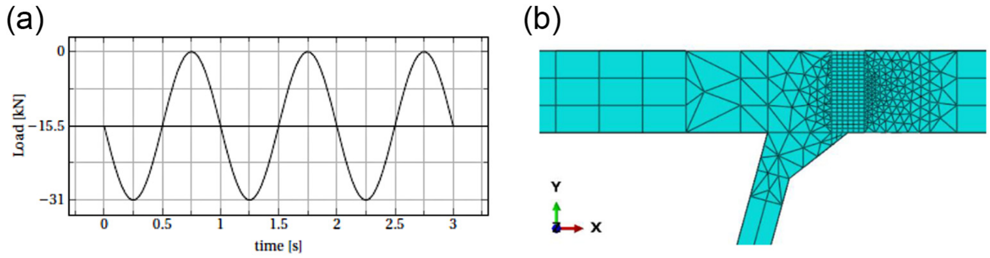

Fig. 23. a) Direct cyclic load. b) Mesh around crack region.

Table 3
Paris law parameters.

C_3	C_4	G_I	G_{II}	G_{III}	$\alpha_{m/n/o}$
$3.00 * 10^{-5}$	1.5	6.3	6.3	6.3	1

The crack propagation rate of the base model is slightly faster compared to the experiment. However, the trend of the graph is comparable with the experiment until around 6 mm of crack depth. The crack propagates slower compared to the experiment after 6 mm of depth in the base model (no residual stresses). It can be noticed that the base FEA and the FEA including all residual stress components, propagates

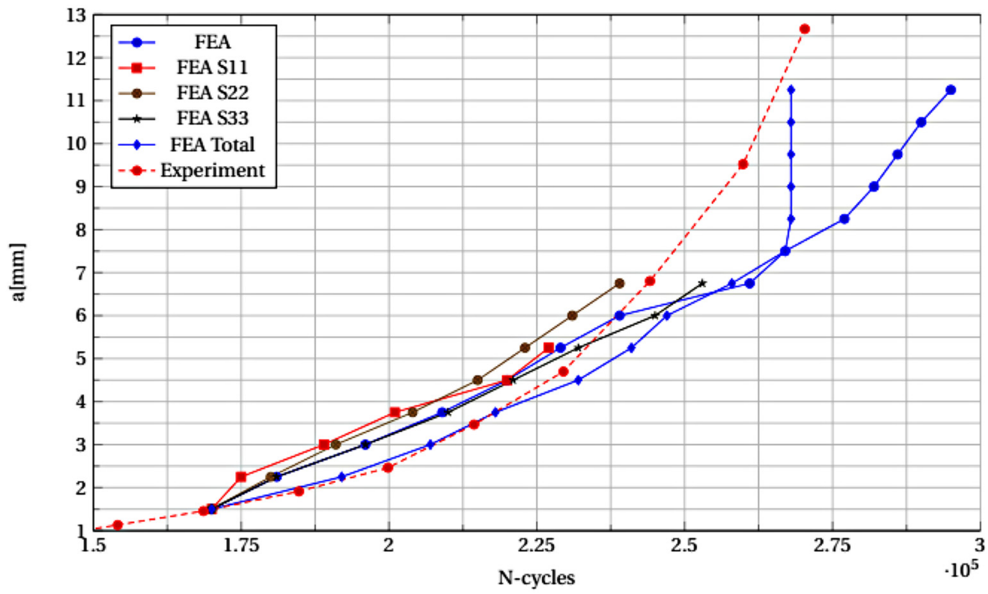

Fig. 24. Results of crack depth propagation model compared to crack depth in [17].

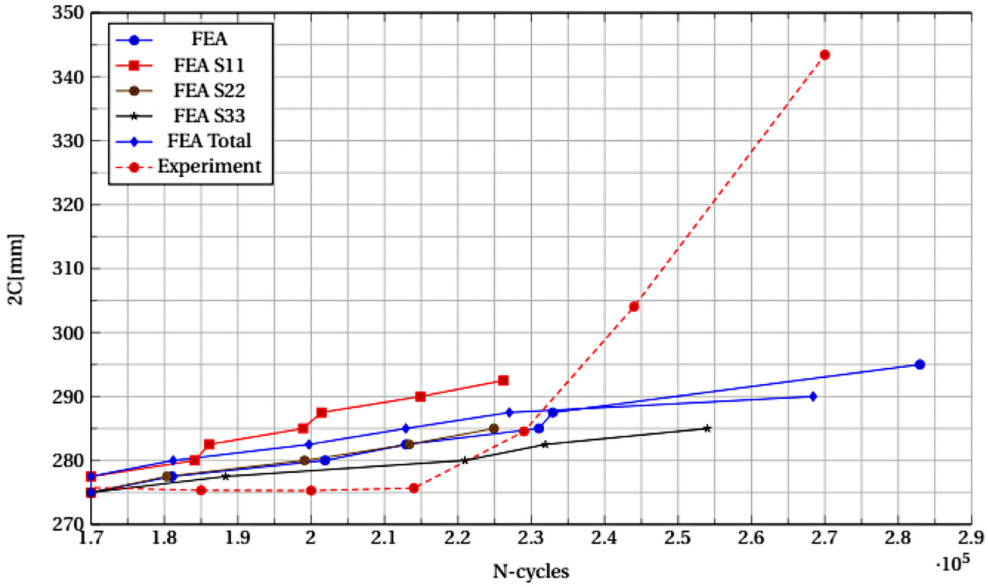

Fig. 25. Results of the crack length propagation compared to the crack length in [17].

further compared to the other models. Computation to the failure requires much more CPU-time compared to the S11, S22 and S33 FEM-models. Therefore, it is chosen to compute only the base model and the model including all three residual stress components. It can be assumed that the other models will show continuous trend as the base FEA and the analysis including all three stress components.

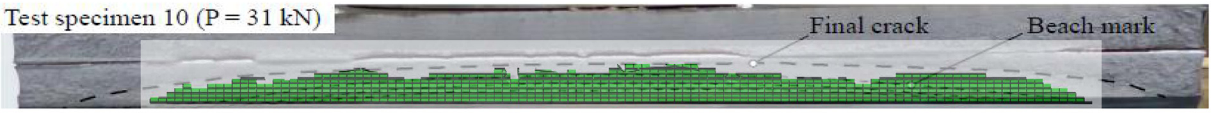

(a) Without residual stress

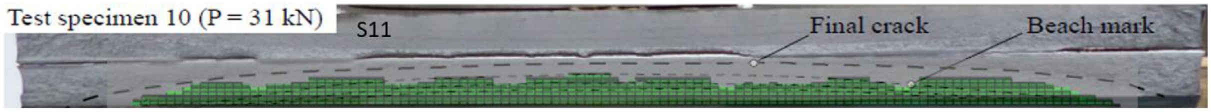

(b) With residual stress component S11

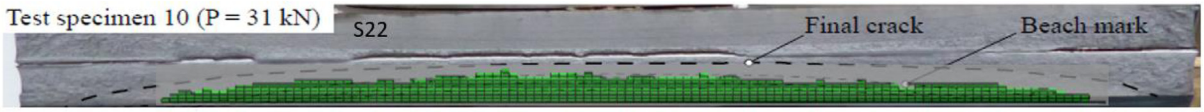

(c) With residual stress component S22

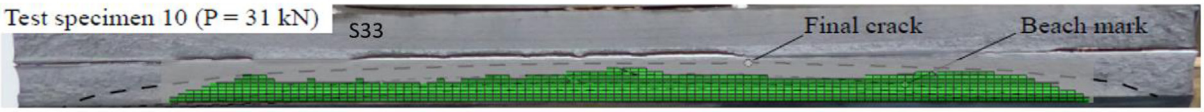

(d) With residual stress component S33

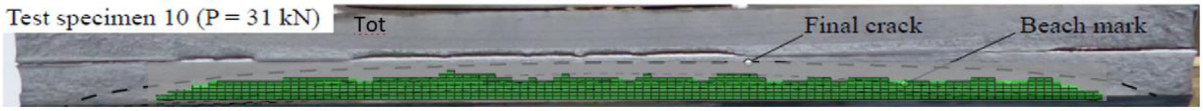

(e) With all residual stress components

Fig. 26. Overlay beach mark measurements [17] & XFEM model with and without residual stresses at a = 6.75 mm.

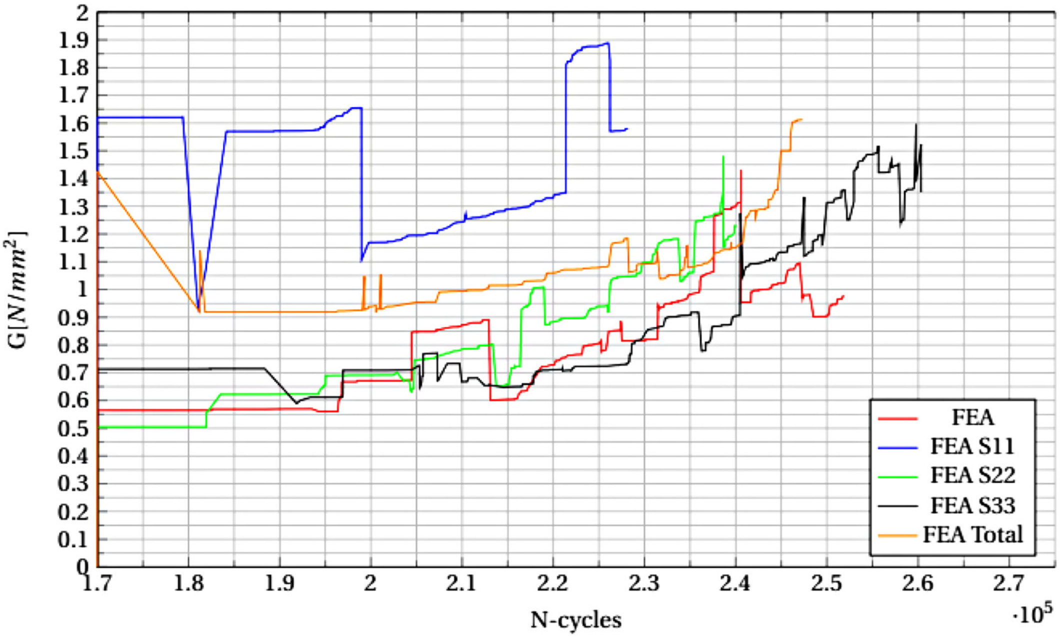

Fig. 27. Results energy release rate fracture mode I.

The crack length (2C) of the base model is comparable until around $2.35 * 10^5$ cycles. After this number of cycles, the experiment propagates to around 345 mm in length, while the FEM-model only slightly propagates in this direction. At last, it can be seen in Fig. 26. that the crack shape between the experiment and the crack simulation analysis is similar. The overall crack shape, including the residual stress components, is similar to all XFEM-models.

The imported residual stress component S11 results in a higher crack propagation rate in terms of crack depth, which is caused by the tensile stress around the weld toe. In the first phase of the crack propagation, the rate of propagation is accelerated as the tensile stress component opens the crack. As the crack propagates towards the region of compressive residual stresses, the crack propagation rate slows down. At the end of the analysis, the relation between the load cycles and the crack depth is similar compared to the base model. The residual stress component S11 on the crack length (2C) results in a higher crack propagation rate. However, the results are still not fully consistent to the experimental data.

The imported residual stress component S22 result in a slightly higher crack propagation rate, which is caused by the tensile stress around the initial fracture in the OSD-specimen. Over the whole analysis, the crack propagation rate is higher compared to the base model. Residual stress component S22 does not have a significant effect on the

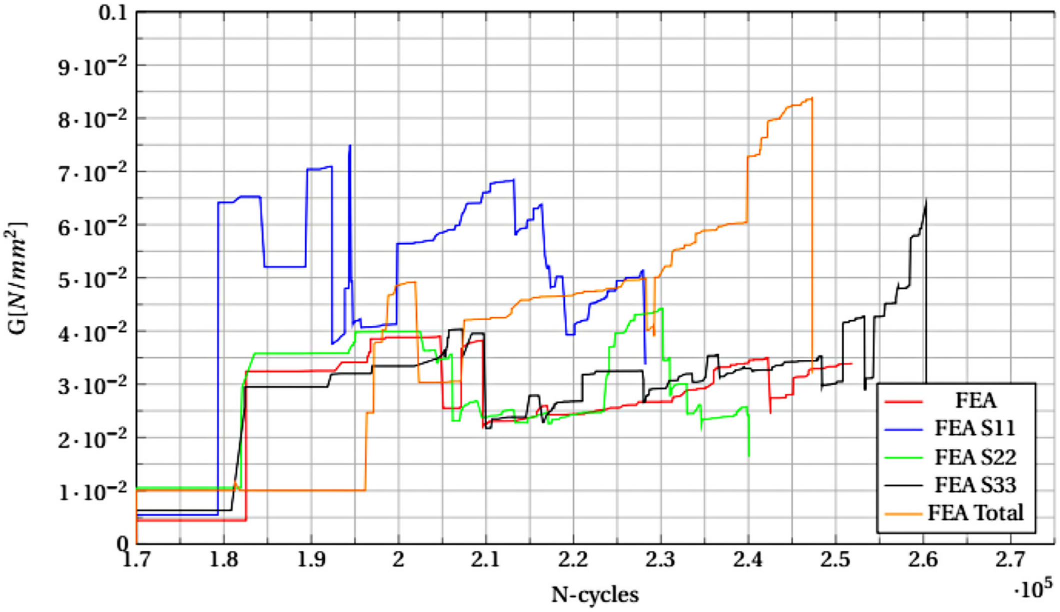

Fig. 28. Results energy release rate fracture mode II.

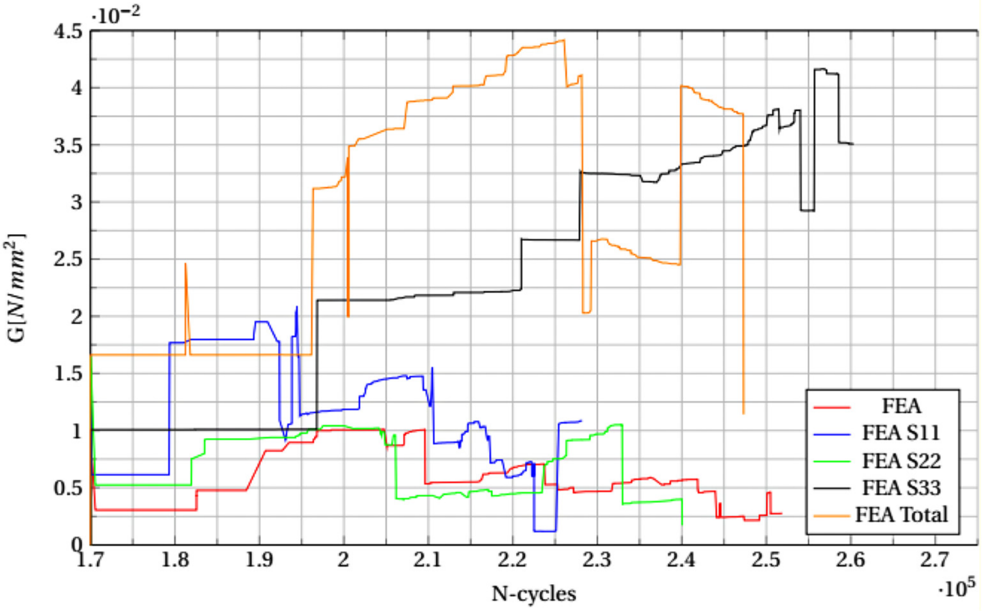

Fig. 29. Results energy release rate fracture mode III.

crack length, as the data are comparable with the base XFEM-model without residual stresses.

The imported S33-stresses result in a slower crack propagation rate, which is likely caused by the tensile stress around the weld zone. As residual stress component S33 is parallel to the crack length, these tensile stresses in the z-direction, close the crack and therefore it requires more cycles, to propagate the crack. Residual stress component S33 results in a lower crack propagation rate in terms, as the specimen hardly propagates in the length.

The FEA, including all three residual stress components, follows the experimental data rather closely, especially between 1.5 mm and 3.75 mm of crack depth. After this crack depth, the crack propagation rate is lower compared to the experimental data. At around 265.000 cycles the FEM-model stopped converging. The moment of failure is around the same number of cycles. Around 235.000 cycles the crack propagation rate is lower compared to the experiment until the point of failure. This can be explained by the perfect material used in FEM-model and therefore the model fails in a few load cycles. In reality, there are small imperfections which declare the steadier crack propagation trend at failure. The results of the crack length are between residual stress component S11 and the base FEA and do not correspond well to the experimental data. This needs further studies.

In Figs. 27 - 29, the fracture energy release rate per fracture mode is shown. Overall, it can be seen that fracture mode 1, shown in Fig. 27, is dominant over fracture modes 2 and 3. Fracture mode 1, crack opening, corresponds to the crack propagation perpendicular to the crack face. Fracture modes 2 and 3 correspond to in-plane shear and out-of-plane shear, respectively. The inserted residual stresses cause higher fracture release rates compared to the base FEA in all three fracture modes. In the dominant fracture mode 1, the residual stress component S11 results in the highest energy release rate. This can be explained by the tensile stress component perpendicular on the crack surface causing the crack to open. The effect of residual stress components S22 and S33 are minimal as the results of these two FE-analysis are close to the base FEA. The model with all the residual stress components is in between the model with the residual S11-component and the other two residual component models. The residual stress component S11 results in high energy release rates in fracture mode 2, in-plane shear. Influence of the residual stress components S22 and S33 are minimal as the results of these two FE-analysis are close to the base FEA.The model with all the residual stress components leads to results of the model with the residual S11-component and the other two residual component models. Fracture mode 2 is influenced by in-plane shear stresses, which correspond with S12-stresses in Abaqus. From the results, it can be explained that the inserted S11-component influences the S12-stresses around the crack region, which results in higher energy release rate. At last, residual stress component S33 results in the highest energy release rate in fracture mode 3. This mode is affected by out-of-plane shear which corresponds to S13-shear stresses in Abaqus. The tensile residual stress component S33 cause an increase in S13-shear stresses. The effect of residual stress components S11 and S22 are minimal as the results of these two FE-analysis are close to the base FEA, while the model which includes all three residual stress components follows the same trend as the residual stress S33 model.

The results above are used to quantify the effect of the residual stresses. In Tables 4 and 5 the average percentage differences and squared correlation (R^2) of each model based on the crack-length/crack-depth is determined and compared to the experiment [17] and the base model without residual stresses. Both data shown in Tables 4 and 5 are determined using the formulas in equations11 and 12. Noted that the crack length is not propagated after only involving S11

Table 4
Average percentage differences between experiments and different FE-models.

Crack length[2C]/Crack depth[a]				
%-difference	FEA base	FEA S22	FEA S33	FEA Total
Experiment	−0.06%	0.52%	−1.34%	1.84%
FEA base	0.00%	0.00%	−0.55%	1.91%

Table 5
Squared correlation between experiments and different FE-models.

Crack length[2C]/Crack depth[a]				
R^2	FEA base	FEA S22	FEA S33	FEA Total
Experiment	65.49%	66.63%	91.65%	59.12%
FEA base	100.00%	100.00%	75.21%	94.70%

residual stress, the quantified comparison of S11 residual stress is not listed in Tables 4 and 5.

$$R^2 = \left(\frac{n\left(\sum xy\right) - \left(\sum x\right)\left(\sum y\right)}{\sqrt{\left[n\sum x^2 - \left(\sum x\right)^2\right]\left[n\sum y^2 - \left(\sum y\right)^2\right]}} \right)^2 \tag{11}$$

$$\%-difference = \frac{\sum_{i=1}^{n} \frac{(y_i - x_i)}{x_i}}{n} \tag{12}$$

To compare the models, the experimental data has been interpolated to increments of 0.75 mm in crack depth and 2.5mm in crack length, as this corresponds with the results of the FEA due to the mesh size of 0.75 mm. Next, the percentage difference compared to the experiment and the base model is computed and averaged. Faster crack propagation results in a negative percentage difference, while a slower crack propagation results in a positive percentage difference. The average difference per model is shown in Tables 4 and 5. The squared correlation compared to the experiment and the base model is calculated. For equal comparison of the 'FEA Total' and 'FEA' models with the other models, the crack depth data till 6 mm is used. Influence of the inserted residual stresses compared to the base model is large, as the average percentage difference is 2% and the square correlation is relatively low at 94%. Residual stress components S33 result in a higher crack propagation rate and therefore result in a lower fatigue life. While the model including all residual stress components results in a lower crack propagation rate and therefore a higher fatigue life.

The base model has a relatively low squared correlation of 65% compared to the experimental data. The crack propagation rate is higher as the average percentage difference is -0.1%. The models including residual stress components S22 and S33 resulted in a higher squared correlation compared to the experimental results. This shows that including these components will improve the results compared to the experimental data [17].

It is concluded that the model, including residual stress components, corresponds well with the experimental data.

4. Conclusions and recommendations

The following conclusions are made based on the results of FE modelling of the welding process and the crack propagation:

- A FE model including shrinkage due to welding has been made to predict and validate the residual stress field of the OSD. The validation of residual stresses is made comparing measured data at the surface of the OSD and over the thickness of the deck flange.
- The thermomechanical FEA resulted in a residual stress field of the OSD-specimen. Simplified residual stress field for each component of the global stress direction is successfully accomplished and these results are used as input for modelling of the fatigue crack propagation.
- he model, including residual stress components, corresponds well with the experimental data. FEA that includes residual stress components in a fatigue crack propagation analysis will improve the results compared to the crack propagation analysis without residual stresses.

5. Recommendations

- The crack length propagation does not correspond satisfactory to the experimental data, while the crack depth does [25]. There is potential for improvement of FEA by apply more releastic boundary conditions thourgh modelling the real loading set up in the future study.
- The solid state phase transformation will affect the dislocation density and the strain hardening, leading to a different local residual stress distribution. This effects will be further considered in the future study.

Data availability statement

The data will be made available upon request.

Declaration of competing interest

The authors declare that they have no known competing financial interests or personal relationships that could have appeared to influence the work reported in this paper.

References

[1] M.H. Kolstein, Fatigue Classification of Welded Joints in Orthotropic Steel Bridge Decks, TU Delft, 2007.
[2] H. Xin, M. Veljkovic, Fatigue crack initiation prediction using phantom nodes based extended finite element method for S355 and S690 steel grades, Eng. Fract. Mech. (2019) 164–176.
[3] H. Xin, J.A. Correia, M. Veljkovic, Three-dimensional fatigue crack propagation simulation using extended finite element methods for steel grades s355 and s690 considering mean stress effects, Eng. Struct. (2020)https://doi.org/10.1016/j.engstruct.2020.111414 vol. In press.
[4] B. Ji, R. Liu, C. Chen, H. Maeno, X. Chen, Evaluation on root-deck fatigue of orthotropic steel bridge deck, J. Constr. Steel Res. 90 (2013) 174–183.
[5] P. Withers, H. Bhadeshia, Residual stress part 2 – nature and origins, Mater. Sci. Technol. 17 (2001) 366–375.
[6] K. Spyridoni, H. Xin, M. Veljkovic, H. Hermans, Calibration of welding simulation parameters of fillet welding joints used in an orthotropic steel deck, ce/papers 3 (3–4) (2019) 49–54.
[7] J. Burk, F. Lawrence, Influence of bending stresses on fatigue crack propagation life in butt joint welds, J. Weld 56 (1977) 61–66.
[8] G. Webster, A. Ezeilo, Residual stress distributions and their influence on fatigue lifetimes, Int. J. Fatigue 23 (2001) 375–383.
[9] C. Cui, Y. Bu, Y. Bao, Q. Zhang, Z. Ye, Strain energy-based fatigue life evaluation of deck-to-rib welded joints in OSD considering combined effects of stochastic traffic load and welded residual stress, J. Bridg. Eng. 23 (2) (2018) 04017127.
[10] H. Xin, M. Veljkovic, Residual stress effects on fatigue crack growth rate of mild steel S355 exposed to air and seawater environments, Mater. Des. (2020) 10872.
[11] H. Xin, M. Veljkovic, Effects of residual stresses on fatigue crack initiation of butt-welded plates made of high strength steel, The seventh international conference on structural engineering, mechanics and cumputation SEMC2019, 2019.
[12] T. Teng, C. Fung, P. Chang, Effects of residual stresses on fatigue crack initiation of butt-welded plates made of high strength steel, Int. J. Press. Vessel. Pip. 79 (7) (2002) 467–482.
[13] Y. Dong, Y. Garbatov, C. Guedes Soares, Fatigue crack initiation assessment of welded joints accounting for residual stress, Fatigue Fract. Eng. Mater. Struct. 41 (8) (2018) 1823–1837.
[14] D. Tchoffo Ngoula, H.T. Beier, M. Vormwald, Fatigue Crack Growth in Cruciform Welded Joints: Influence of Residual Stresses and of the Weld Toe Geometry, 2017.
[15] S. Taheri, A. Fatemi, Fatigue Crack Behavior in Power Plant Residual Heat Removal System Piping Including Weld Residual Stress Effects, 2017.
[16] C. Acevedo, A. Nussbaumer, Influence of welding residual stresses on stable crack growth, Tubular Structures XIII - Proceedings of the 13th International Symposium on Tubular Structures, 2010.
[17] W. Nagy, Fatigue assessment of orthotropic steel decks based on fracture mechanics, UGENT, Gent 2017.
[18] NEN, NEN-EN 1993-1-2, 2011.
[19] Oerlikon, Fluxocord 31 HD, [Online]. Available: http://www.oerlikonline.hu/files/510.pdf.
[20] J. Goldak, A. Chakravarti, M. Bibby, A new finite element model for welding heat sources, 1984.
[21] W. Nagy, B. Wang, C. Bohumil, P.v. Bogaert, H.D. Backer, Developement of a fatigue experiment fir the stiffener to deck plate, Intern. J. Steel Struct. 17 (2017) 1353–1364.
[22] S. Kainuma, Y. Jeong, M. Yang, S. Inokuchi, Welding residual stress in roots between deck plate and U-rib, Measurement (2016) 92.
[23] Dassault systemes, Abaqus V. 6.19 documentation, 2016.
[24] F. Bozkurt, E. Schmidova, Fracture Toughness Evaluation of S355 Steel Using Circumferentially Notched Round Bars, 2018.
[25] B. Wang, W. Nagy, H.D. Backer, A. Cheng, Fatigue process of rib-to-deck welded joints of orthotropic steel decks, Theor. Appl. Fract. Mech. 101 (2019) 113–126.